Rare Metal Materials and Engineering

Available online at **www.rmme.ac.cn**

Science Press

Cite this article as: Rare Metal Materials and Engineering.

ARTICLE

DOI: 10.12442/j.issn.1002-185X.20240453.

Research on the near βtitanium alloy with high strength obtained by composition design and intermediate annealing process

Jiang Shihui[1], Di Jinnan[2], Xu Zaidong[3], Sun Saihua[3], Mao Pingli[1]✉

[1] School of Materials Science and Engineering, Shenyang University of Technology, Shenyang 110870, China；

[2] Guidaojiaotong Polytechnic Institute, Shenyang 110230, China；

[3] Northeastern University, Shenyang 110000, China

Abstract: In this work, a near β-type Ti-5.5V-4Mo-2.2Cr-Fe-3.6Al alloy was designed based on the multi-alloying principle of critical molybdenum equivalent ([Mo]eq), combined with parameters such as electron concentration (VEC), Bo-Md that can influence the stability of β phase. The alloy was subjected to solid solution, intermediate annealing during the rolling process, and aging treatment. The microstructure and mechanical properties of the alloy were analyzed. The results showed that martensitic transformation occurs in the alloy during rolling. The grain size of the alloy after annealing during the rolling process is only 38 μm, due to the martensite has a hindrance to grain boundary migration. Then it has good strength-plasticity matching, the tensile yield strength reaches 1050 MPa and the elongation is more than 15%. A large number of α phases are precipitated in the microstructure of the rolled alloy after aging treatment, which further improves the properties of the alloy. The strength of the alloy exceeds 1500 MPa and the elongation is more than 5%.

Key words: Near β titanium alloy; Cold rolling; Annealing; Tensile properties

Titanium alloys are widely used in aerospace, automotive and other important industrial fields due to their high strength and good corrosion resistance[1-7]. Among them, the β-type titanium alloy has good plasticity in the solid solution state, and has ultra-high specific strength and good corrosion resistance after aging, which is attractive to the material research field. Now it has been applied to the structural parts of large aircrafts, for example Ti1023（Ti-10V2Fe3Al）alloy and Ti55531（Ti-5Al5Mo5V3Cr1Zr）alloy[9-12]. Especially for near β titanium alloy, due to its critical composition and good aging precipitation ability, the alloy can obtain a strengthening effect of 400~700 MPa after aging[13-17]. Zhang et al.[18] showed that the volume fraction of α phase in near β titanium alloy after aging treatment was high, about 42 % ~ 80 %, and the average size was 35~150 nm, a large number of fine α phases increase the strength to 1600 MPa. With the rapid development of the aerospace industry, the demand for the service strength of titanium alloys is increasing, and the performance of titanium alloys is further improved, then the properties of the alloy are improved from the perspective of composition design and heat treatment process in this paper.

The composition design of near β titanium alloys generally adopts the principle of diversification of critical composition, Under the condition that the molybdenum equivalent of the alloy is at the critical molybdenum equivalent, several β-type stabilizing elements V, Mo, Cr, Fe and α-type stabilizing element Al are added appropriately. Li et al.[19] designed Ti-5.2Mo-5.2Cr-4.0Al-4.4V-2.4Nb alloy based on this concept, the strength of the alloy can reache 1560 MPa after aging. Coffgniiez et al.[20] designed a metastable β-type titanium alloy using electronic parameters such as Bo and Md, the alloy has a good performance. This indicates that molybdenum equivalent ([Mo]eq) and electronic parameters such as Bo and Md can effectively predict the stability of β phase after aging. Therefore, according to the above design method, a near β-type titanium alloy with a nominal composition of

Received date:

Foundation item: 14th Five-Year Plan of Liaoning Province Education Science(JG22EB103)

Corresponding author: Mao Pingli,Prof. School of Materials Science and Engineering, Shenyang University of Technology, Shenyang 110870, China

Ti-5.5V-4Mo-2.2Cr-1Fe-3.6Al(wt.%) was designed in this work. At the same time, the electronic parameters such as electron concentration, Bo and Md of the alloy were considered. The nominal composition is Ti-5V-2Mo-2Cr-1Fe-6Al(at.%).

The β phase in the near β-type titanium alloy is more metastable than in the metastable β-type titanium alloy, and the martensitic transformation is easy to occur during the deformation process, which can increase the hardening rate of the alloy during the deformation process. At the same time, the generation of martensite is also conducive to grain refinement during annealing, it can synergistically improve the strength and plasticity of the alloy. Therefore, we need to use different cold rolling combined with annealing process to refine the grain of the alloy. Zhang et al. [21] prepared a high-strength β-type titanium alloy by cold rolling and annealing treatment. According to the experience of related rolling and heat treatment processes, the effects of annealing after different cold rolling deformation, single annealing and intermediate annealing processes on the microstructure of the alloy were compared in this study, and the related processes for obtaining fine β grain structure were explored.

Combined with the above research, a new near β-type Ti-5.5V-4Mo-2.2Cr-1Fe-3.6Al(wt.%) alloy was designed according to the molybdenum equivalent and electronic parameters such as electron concentration and Bo-Md in this study, and the alloy was subjected to intermediate annealing and aging treatment during rolling. It provides a reference for the composition design of near β-type titanium alloy and the synergistic improvement of strength and plasticity by rolling and heat treatment.

1 Experiment

1.1 Alloy design

Commercial metastable β-type titanium alloys with good properties generally contain V, Mo, Cr and Fe elements, such as Ti-1023 (Ti-10V-2Fe-3Al) alloy and Ti55531 (Ti5Al5V5Mo3Cr1Zr) alloy. V and Mo are β-phase stable elements of the same crystal type, and they are infinitely miscible with Ti in the crystals of BCC and HCP structures. Therefore, there is no clear constraint on the content of V and Mo in the alloy composition design. In order to avoid the formation of Ti Cr_2 intermetallic compound during the aging process, Cr addition is generally not more than 3%, because it is a slow eutectoid element. As Fe is a fast eutectoid element, it is easy to produce compounds such as TiFe and $TiFe_2$ during the aging process, and the segregation of Fe element is also easy to cause β spots, so the addition amount should be less than or equal to 2%. In addition, in order to improve the precipitation ability of α phase and avoid the generation of precipitate-free zones at grain boundaries, 3% Al is generally added to titanium alloy. Based on the above factors, in order to give full play to the alloying effect of each element, the alloy composition design comprehensively selects elements such as V, Mo, Cr, Fe and Al.

[Mo]eq, VEC and Bo-Md are all related to the structural stability and final properties of metastable β-type titanium alloys. They are also the most commonly used parameters in the composition design of metastable β-type titanium alloys. They can be used as conditions to constrain the content of components and further determine the element content of the alloy. When the molybdenum equivalent is close to the critical molybdenum equivalent of 10, the stability of the β phase is considered to be the lowest, and the alloy has the strongest aging precipitation ability. Therefore, the molybdenum equivalent value of 10 should be taken as the target molybdenum equivalent. The calculation formula of molybdenum equivalent is expressed as:

$$[Mo]eq=1.0(wt.\%Mo)+0.67(wt.\%V)+0.44(wt.\%W)+0.28(wt.\%Nb)+0.22(wt.\%Ta)+2.9(wt.\%Fe)+1.6(wt.\%Cr)+1.54(wt.\%Mn)+1.25(wt.\%Ni)-1.0(wt.\%Al) \quad (1)$$

Since the valence electron concentration VEC is related to the structural stability of titanium alloys and the properties of the β phase, it has been confirmed by a large number of experiments[19-22]. Therefore, in the process of composition design, VEC is also considered to be one of the physical parameters affecting the stability of β phase in Ti alloy. Same as the molybdenum equivalent, the structural stability of the β-phase solid solution is low when the VEC value is small. Twinning and phase transformation are easy to occur during the tensile process to increase the hardening rate of the alloy deformation, which also helps to improve the toughness of the alloy. Therefore, this paper selects the VEC value as 4.10. In eq.(2) the VEC is expressed as:

$$\frac{e}{a} = \sum_{i=1}^{n} X_i N_i \quad (2)$$

where X_i (i = 1,2,3,4) represents the molar concentration of elements; N_i is the number of valence electrons of each element. In recent years, some studies have used the Bo-Md parameter to predict the phase composition and deformation mechanism of titanium alloys. Bo(Bond order) is used to reflect the strength of covalent bonds formed between Ti and alloying elements, and Md (The Metal d-orbital energy level) is a parameter closely related to the electronegativity of the element and the radius of the metal bond[23]. Fig.1 is a Bo-Md phase diagram showing the (Bo,Md) position of the designed alloy. When the (Bo,Md) value is between the martensitic transformation line (Md=RT) induced by stress and the martensitic transformation start line (Ms=RT) at room temperature, the alloy has better mechanical properties. At this time, the (Bo,Md) value of the alloy is close to that of the commercial near β titanium alloy Ti-10V-2Fe-3Al. Therefore, the target (Bo,Md) values are selected as 2.773 and 2.361, which are close to those of Ti-1023. The calculation formulas of Bo and Md values are as follows :

$$\overline{Bo} = \sum_{i=1}^{n} X_i \ (Bo)_i \quad (3)$$

$$\overline{Md} = \sum_{i=1}^{n} X_i \ (Md)_i \quad (4)$$

Where X_i is the molar concentration of each element in the alloy; $(Bo)_i$ is the Bo value of each element, $(Md)_i$ is the Md value of each element. The positions of (Bo, Md) values of the alloy and some near-β-type alloys with good properties can be marked through calculation, in the stable phase diagrams of $\overline{Bo}$ and $\overline{Md}$ values. As Fig.1 shows:

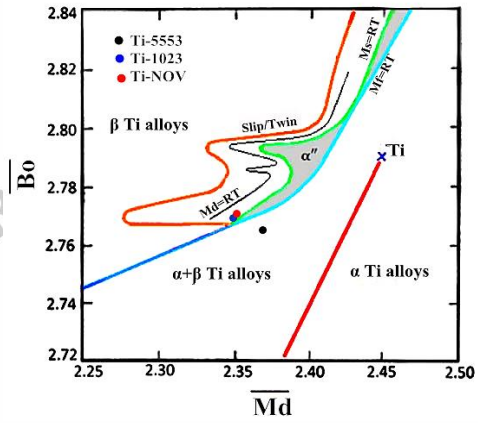

Fig.1 $\overline{B_o}$-$\overline{M_d}$ two-parameter diagram.

According to Eq.(1),(2),(3),(4) and $\sum_{i=1}^{n} C_i = 1$, the nominal composition of the alloy can be calculated as Ti-5.5V-4Mo-2.2Cr-1Fe-3.6Al(wt.%). Table 1 shows the actual composition of the alloy, and the error between each component and the nominal component is less than 1.5%.

Table 1 Chemical composition of the design alloy(wt.%)

V	Mo	Cr	Fe	Al	C	O	H	Ti
5.56	3.97	2.33	1.04	3.04	<0.1	0.11	<0.1	Bal

1.2 Experimental materials and methods

The alloys were prepared using the raw metals of Ti, V, Mo, Cr, Fe and Al with purities exceeding 99.9%. The alloys were prepared through arc-melting for more than six times in an argon atmosphere. Subsequently, and all the ingots (300 g in weight) were homogenized in a vacuum at 1000 ℃ for 24 h, followed by water quenching (WQ). The elements of vanadium, molybdenum, chromium, iron and aluminum in the alloy were determined by infrared analysis. The oxygen content in the alloy was determined by pulse heating inert gas melting infrared absorption method. The homogenized alloy ingot was cut into cuboid samples using electro-discharge machining. The cuboid sample was treated by solid solution and used as the original sample for cold rolling. The phase transition point of the alloy is 840 ℃ measured by metallographic method. In order to avoid the formation of α precipitation phase in the annealing process, the annealing temperature in the intermediate annealing process of the rolling process is selected as 870 ℃ above the phase transition point, and the annealing time is 30min. The process flow diagram of the intermediate annealing process used in this study is shown in Fig.2.

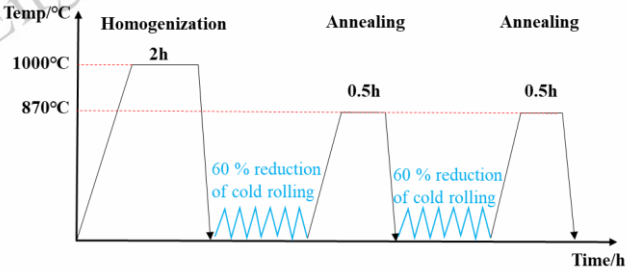

Fig.2 Intermediate annealing process of rolling process.

Samples were mechanically ground and polished, then etched with a solution containing 10%HF + 30%HNO_3 + 60%H_2O. Microstructures were characterized via optical microscopy (Olympus-PMG3) and scanning electron microscopy (SEM, Zeiss Sigma) coupled with electron backscatter diffraction (EBSD) and energy-dispersive X-ray spectroscopy (EDS). Additionally, sub-microstructures were characterized via transmission electron microscopy (TEM,JEM-2100F). X-ray diffraction (XRD) was applied to identify phases in the alloys by using a SmartLab(9) diffraction instrument with an incident beam of Cu-Kα radiation. Scanning was performed from 20°~100° at a scanning rate of 5°/min. The SEM specimens were initially polished by 3000-grit SiC papers, and then electrochemically polished for the final surface clarification using a solution composed of methanol, n-butanol, ethylene glycol butyl ether, and perchloric acid (6.5: 2: 1: 0.5) at a direct voltage of 25V and a temperature of ~253K. TEM specimens were punched to Φ3 mm plate sheets and then mechanically ground to ~55μm in thickness, and then subjected to twin-jet electro-polishing using a solution of HClO4:C2H6O = 1:8 at the temperature of about 248K. The tensile tests were carried out on a CMT-5305GL universal electronic tensile testing machine with a strain rate of 1×10^{-3} s^{-1} at room temperature. Three samples of each alloy were used to determine the tensile properties, and the averaged results were adopted.

2 Results

Fig.3(a) shows the microstructure of the as cast state has coarse grains, with strip-shaped α precipitates distributed within the grains. Due to the low melting point alloying elements such as Al being prone to segregation at grain boundaries, α phases are prone to precipitate at grain boundaries, which can cause brittle fracture of the alloy during deformation. Therefore, it is necessary to eliminate element segregation by homonization. Fig.3(b) and (c) show the OM and SEM images of the alloy after homogenization at 1000℃/2h. The figures indicate that the α phase present in the as cast state has been dissolved into the matrix. The XRD results in Fig.3(b)

also demonstrate that only a single BCC structure after homomization. SEM-EDS results indicate that the distribution of various alloying elements in the alloy after homogenization is uniform which is beneficial for the uniform distribution of α phase after aging.

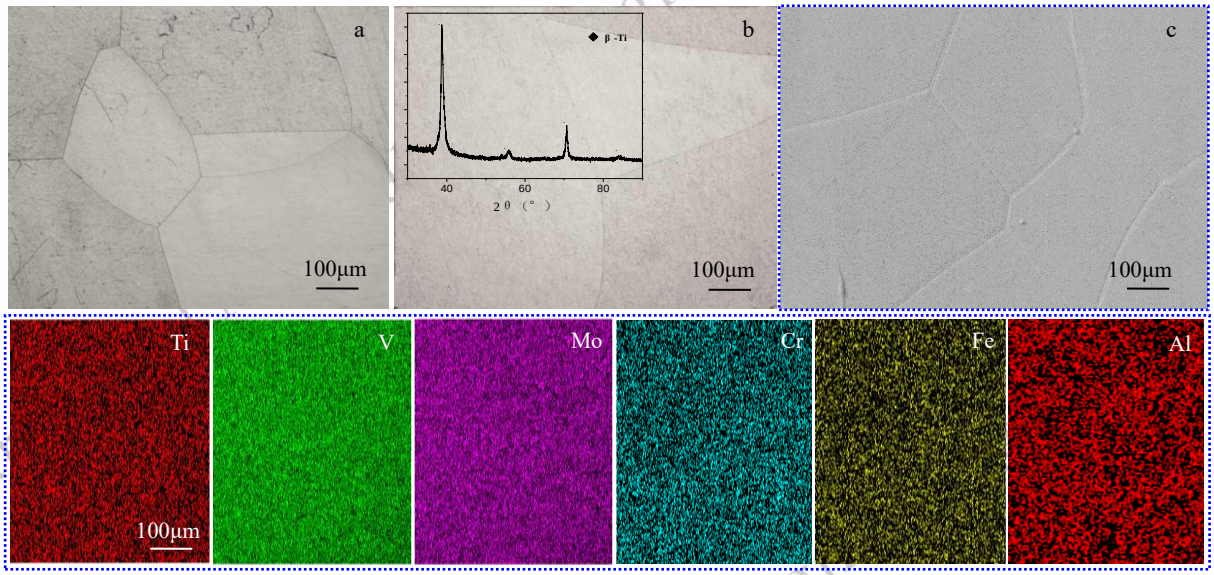

Fig.3 OM of as cast alloy(a), OM and XRD pattern of homogenized alloy(b) SEM image of homogenized alloy(c)

Fig.4 presents the XRD patterns of the alloy after cold rolling with different reductions. The microstructure of the alloy after cold rolling with a 30% reduction is entirely composed of a single BCC structure. After increasing the cold rolling reduction to 60%, in addition to the β matrix, hexagonal martensite phase precipitated in the microstructure, which increased the hardening rate in cold rolling process and hindered further cold rolling deformation. Fig.5 shows the deformation OM structure with different cold rolling reductions and the recrystallized OM structure after annealing at 870℃/30 min, as well as the corresponding IPF image. Fig.5(a) shows that the grain size of the alloy remains almost unchanged after cold rolling with a 30% reduction, and a large number of slip lines appear inside the grains. However, the internal deformation of the alloy is uneven, and the number of slip lines generated inside different grains varies greatly. After annealing and recrystallization, the grain refinement of the alloy is relatively small. According to the IPF image, the grain size of the alloy after annealing is approximately 150μm. Fig.5(b) shows that the grains undergo a certain degree of deformation after cold rolling with a 60% reduction, and the grains after annealing and recrystallization are relatively uniform. According to IPF image, the average grain size of the alloy after 60% cold rolling and annealing is about 75μm. The microstructure of the alloy after secondary cold rolling with 60% reduction and annealing after cold rolling is shown in Fig.5(c), where smaller grains undergo a certain amount of deformation. After annealing and recrystallization, the grains are further refined. According to the IPF image, the average grain size of the alloy is 38μm after intermediate annealing after cold rolling

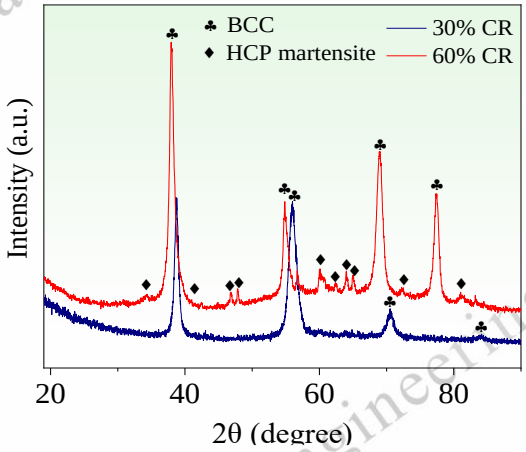

Fig.4 XRD pattern of the alloy after cold rolling with 30% and 60% reduction

Fig.6 presents the TEM bright field(BF) image, dark field(DF) image, and corresponding selected area electron diffraction(SAED) patterns after cold rolling with a 60% reduction. The SAED pattern of the corresponding blue circle area in Figure 6(a) shows that the bright field corresponding region is the β phase with BCC structure. There are a large number of sub-grains with a size of about 80nm, which are formed due to the dislocation movement after cold rolling. From Fig.6(c) the DF image and corresponding SAED pattern of Fig.6(d), it can be concluded that the HCP-structured α' martensite precipitates in the microstructure of the alloy after cold rolling with 60% reduction.

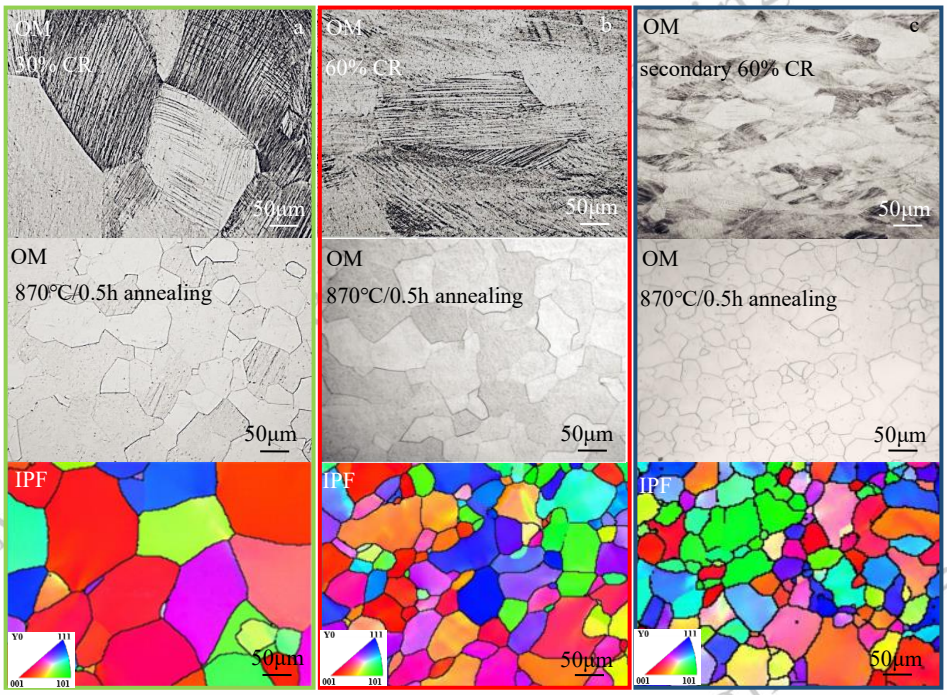

Fig.5 OM image of the alloy after cold rolling; OM image and IPF diagram after annealing

The diffraction pattern of the α' phase has shown a ring-shaped pattern, indicating the presence of many nanoscale small grains with different orientation inside the α' phase which indicates that a large number of dislocations pass through the α' phase during the cold rolling process and form small grains in the α' phase. During the cold rolling process, titanium alloys with a near β shape generally produce an orthogonal structure of α" martensite phase. However, the reason for the formation of hexagonal martensite phase in this experiment may be due to the transformation from orthogonal martensite phase to hexagonal martensite phase during the cold rolling process. The formation of martensite phase will increase the hardening rate during cold rolling, increasing the dislocation density, and hinder the growth of grains during annealing to refine the grains after annealing[24].

Fig.7 shows the microstructure of the annealed alloy after aging at 520℃~580℃/2~8h, as well as the corresponding XRD patterns, and the SEM images after aging at 520℃/8 hours and 550℃/8h. Fig.7(o) shows the XRD patterns after aging at 520 ℃~580℃ for 4 hours. It can be seen that there are HCP-structured α and BCC-structured β phases after aging at 550℃ and 580℃, while in the microstructure after aging at 520℃/4 hours, in addition to α and β phases, there are also Ω phases. From the optical structure of the alloy in Figures 7(a)~(l) after aging at different temperatures and times, it can be seen that with the increase of aging temperature and time, the distribution of α phase becomes more uniform, and the size of α phase gradually increases. After 550℃/8 h, the distribution of α phase in the microstructure is uniform, while the distribution of α phase is not uniform at other aging times, and there are precipitation free zones between grains.

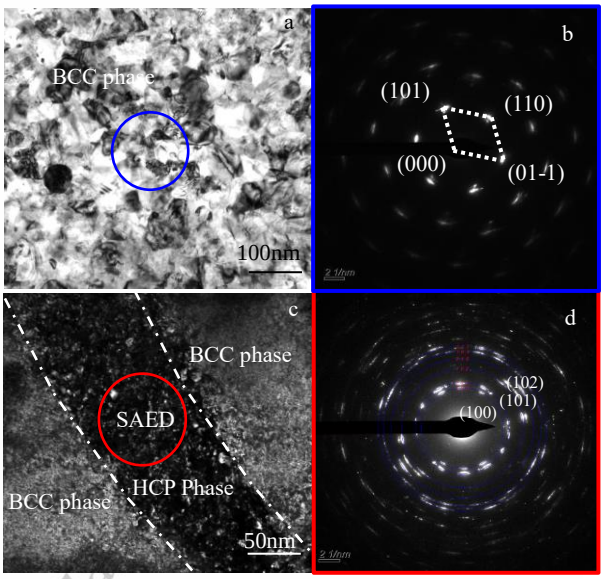

Fig.6 TEM bright and dark field image (BF and DF image) and corresponding selected area electron diffraction pattern (SAED pattern) of the alloy after cold rolling with 60% reduction (a); (b) SAED pattern corresponding to the blue circle area in Fig.6(a); DF image (c); (d) SAED pattern corresponding to red circle area in Fig.6(c).

Therefore, in order to ensure the uniform distribution of α phase, the aging treatment for this experiment is selected at 550 ℃/8h. Fig.7(m) and (n) show the SEM images of the alloy after aging. It can be seen from the images that the size of the α phase after aging at 520℃ shows a triangular distribution, while the distribution of the alloy after aging at 550℃ shows a V-shaped distribution.

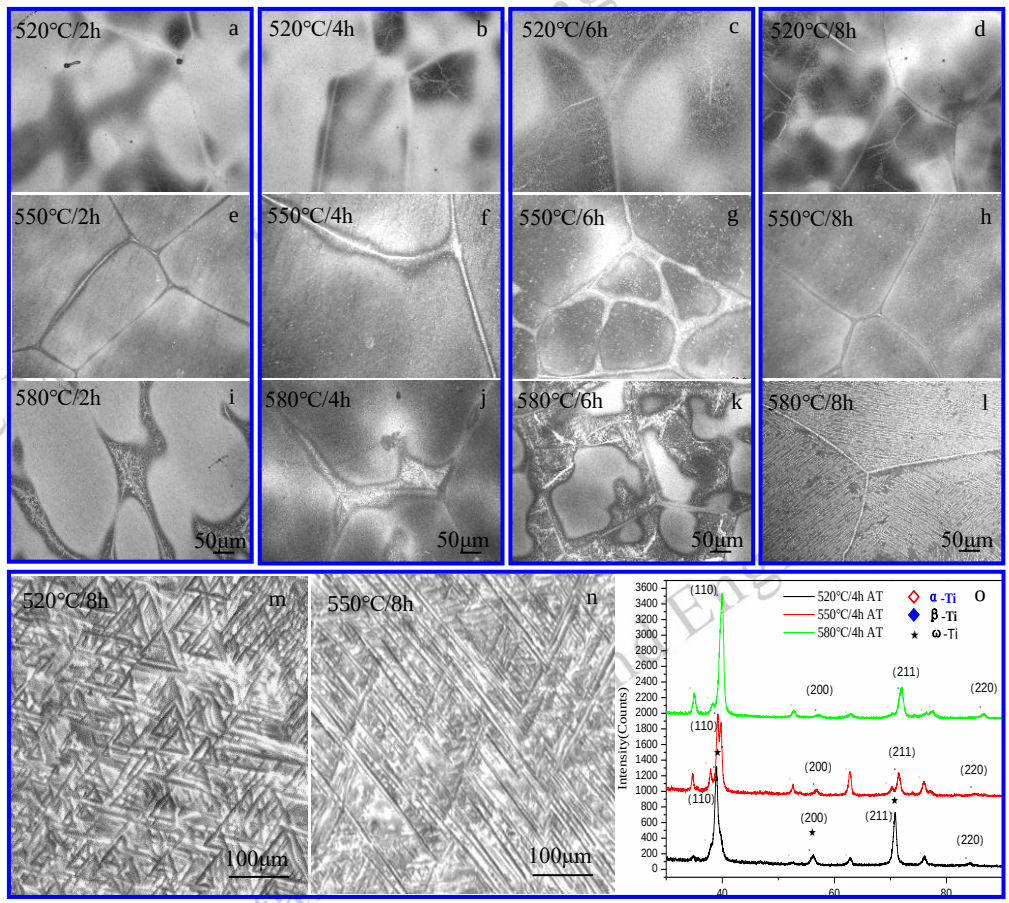

Fig.7 The OM, SEM images and XRD pattern of alloy after aging with different heat treatment. (a)~(l) The OM images of different aging treatment; (m) and (n) SEM images with different aging treatment; (o) XRD patterns of the alloy with different aging treatment.

In order to further demonstrate the microstructure of the α phase after aging at 550℃/8h, we further characterized the aged alloy by TEM. Fig.8 shows the TEM bright field image(BF), high-resolution TEM(HRTEM) image, and strain distribution corresponding to HRTEM image of the alloy after aging treatment at 550℃/8h. It can be seen from the figure that a large amount of white α phase with a width of about 40nm precipitates from three directions in the microstructure of the alloy after aging. Fig.8 (b) shows the HRTEM phase in the local region and the corresponding FFT image in the upper right corner. From fig.8, it can be seen that there is a different orientation of α phase atomic arrangement in the local region, and there is significant lattice distortion between alpha phases with different orientations. The corresponding strain distribution map is highlighted.

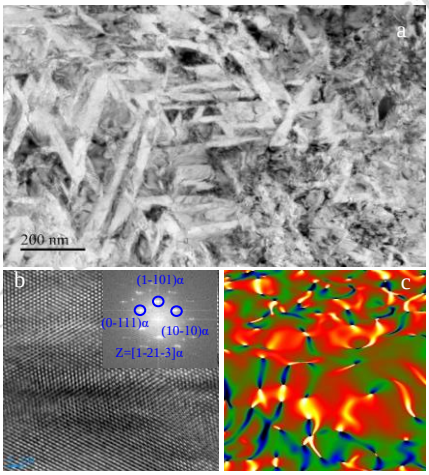

Fig.8 TEM bright field image(a); HRTEM image(b); (c)The strain distribution diagram corresponding to the region of Fig.8(b)

Fig.9 shows the tensile performance curves and corresponding hardening rate curves of the alloy after different rolling, annealing, and aging treatments. It can be seen from the figure that the yield strength of the alloy with a single BCC structure after a single 60% reduction annealing (SCRA) reaches 900MPa, while it has a 14% elongation. The yield strength of the alloy after a second 60% reduction cold rolling annealing (DCRA) reaches 1050MPa, which is 150 MPa higher than that of SCRA. However, the hardening rate curves indicate that the hardening rates of the DCRA are not significantly different. Compared to the already applied Ti-10V-2Fe-3Al alloy, the alloy obtained higher strength after annealing. In addition, the alloy can achieve a yield strength of nearly 1400 MPa while still having a 7% elongation after a single cold rolling annealing and aging at 550℃/8h(SCRAA).

The yield strength of the alloy after annealing during cold rolling and aging at 550℃/8h(DCRAA) is close to 1500MPa, while having an elongation of about 5%. And the alloy after DCRAA has a high hardening rate in the initial deformation stage. The yield strength of the alloy sample after DCRAA is higher than that of the SCRAA. This is not only due to the strengthening effect of finer grains obtained after secondary cold rolling and recrystallization, but also due to the influence of stress and thermal effects, the diffusion of elements in the alloy after secondary cold rolling and recrystallization is more complete, and the distribution of elements in the alloy is more uniform, which will be beneficial to the strength and plasticity of the alloy.

.

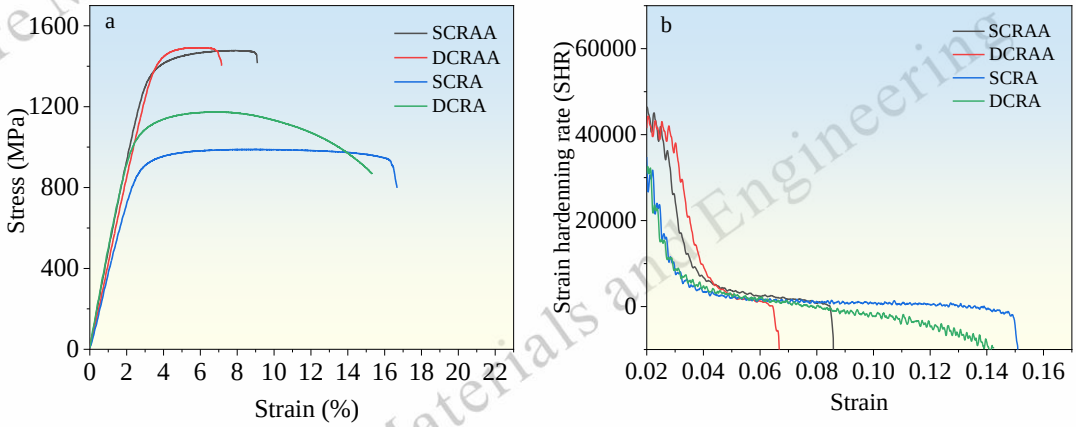

Fig.9 stress-strain curves of the rolled alloy with different heat treatments(a), hardening rate curves of the rolled alloy with different heat.

Fig.10 shows the tensile fracture morphology of the aged alloy of SCRAA and DCRAA. For the SCRAA alloy, the fracture features consist of cleavage platforms and dimples. It can be seen that there are obvious tearing edges on the cleavage surface in Fig. 10(b). DCRAA alloy has fewer cleavage fracture platforms in its fracture morphology compared with SCRAA, which are mainly composed of dimples formed at the interface between α particles and β matrix. These dimples are relatively shallow compared to the dimples of SCRAA alloy, and absorb relatively less energy during the fracture process, which can result in lower fracture toughness of DCRAA alloy compared to SCRAA alloy.

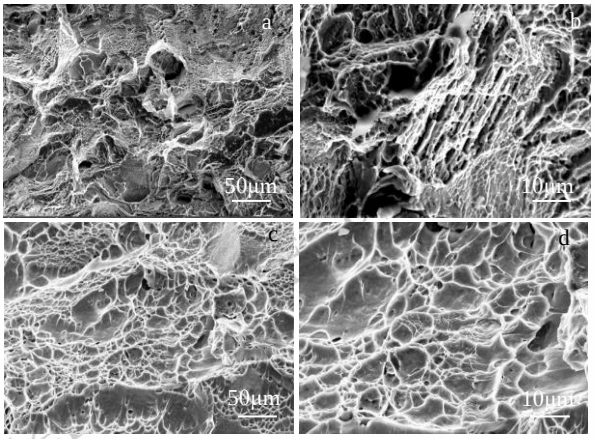

Fig.10 Tensile fracture morphology of alloy samples after aging (a) and (b) SCRAA; (c) and (d) DCRAA.

3 Discussion

The yield strength of titanium alloy after annealing is contributed by the lattice resistance, solid solution strengthening, dislocation strengthening, and grain boundary strengthening of the alloy. After aging, the yield strength of the alloy also exhibits precipitation strengthening on the basis of the strength of the solid solution alloy. Expressed as:

$$\sigma_{YS} = \sigma_0 + \sigma_{ss} + \sigma_{gb} + \sigma_p \quad (3)$$

In the formula, σ_{YS} is the yield strength of the alloy, σ_0 is the lattice resistance of the alloy, σ_{ss} is the contribution of solid solution strengthening, σ_{gb} is the contribution of grain

boundary strengthening, and σ_p is the contribution of precipitation strengthening. $\sigma_0 = \sum_{i=1}^{n} C_i \sigma_{0i}$ is the yield stress of the alloy without strengthening mechanism. C_i and σ_{0i} represent the molar fraction and yield stress of component i in the solid solution, respectively. After calculation, the lattice friction resistance of the alloy is 260MPa. Solid solution strengthening can be described as:

$$\sigma_{ss} = AG[\sum_i \varepsilon_i^2 X_i]^{2/3} \quad (4)$$

Among them, A is the fitting constant (obtained by comparing calculated data with actual data), the value is shown in Table 2, and G is the average shear modulus of the alloy, $G = \sum_i X_i G_{ii}^{(0)}$, X_i is the atomic fraction of component i in the alloy, $G_{ii}^{(0)}$ is the shear modulus of pure i-component. $\varepsilon_i = (\eta_i'^2 + \alpha^2\delta_i^2)^{1/2}$, α depends on the type of dislocation undergoing plastic deformation (usually screw dislocations are taken as 3<α<16, and for edge dislocations, α>16), the value is shown in Table 2. $\eta_i' = \frac{\eta_i}{1+0.5|\eta_i|}$, $\eta_i = \frac{1}{G}\frac{dG}{dX_i}$, is a mismatch in elastic modulus, and its formula is:

$$\eta_i = p\sum_j X_j \delta G_{ij} \quad (5)$$

In the formula, p is the coefficient (For fcc structure p=12/13;for bcc structure p=9/8), where $\delta G_{ij} = \frac{2(G_{ii}^{(0)} - G_{jj}^{(0)})}{G_{ii}^{(0)} + G_{jj}^{(0)}}$, $\delta_i = \frac{1}{S_{lat}}\frac{dS_{lat}}{dX_i}$ is an atomic size mismatch, S_{lat} is the average distance between the nearest atoms in a multicomponent alloy with atomic size mismatch, and δ_i can be expressed by the following formula:

$$\delta_i = p\sum_j X_j \delta R_{ij} \quad (6)$$

p is the coefficient (for fcc structure p=12/13; for bcc structure p=9/8), where $\delta R_{ij} = \frac{2(R_{ii} - R_{jj})}{R_{ii} + R_{jj}}$, $R_{ii} = s_{ii}^{(0)}/2$, $s_{ii}^{(0)}$ is the distance between the nearest equilibrium atoms in the lattice of pure component i. The formula R_{ii} is only valid for alloys with the same lattice type. Correction is required for pure metal elements with different lattices, $R_{ii} = s_{ii}/2$, s_{ii} is the average distance between the nearest atoms of component i in a multi-component alloy lattice, which is effective for different types of lattices. Parameter $K_{lat}^{(s)}$、$S_{lat}^{(s)}$ can be considered as an approximate value of the bulk modulus and average distance between atoms of the multi-component alloy.

$$S_{ii} = \frac{K_{ii}^{(s)} S_{ii}^{(s)^2} + K_{lat}^{(s)} S_{lat}^{(s)^2}}{K_{ii}^{(s)} S_{ii}^{(s)} + K_{lat}^{(s)} S_{lat}^{(s)}} \quad (7)$$

$$K_{ii}^{(s)} S_{ii}^{(s)} = 2m_{lat} n_{lat} f_{lat}{}^3 [X_i K_{ii}^{(0)} S_{ii}^{(0)} / (m_i^{(0)} n_i^{(0)} f_i^{(0)^3})] \quad (8)$$

$$K_{ii}^{(s)} S_{ii}^{(s)^2} = 2m_{lat} n_{lat} f_{lat}{}^3 \left[\frac{X_i K_{ii}^{(0)} S_{ii}^{(0)^2}}{m_i^{(0)} n_i^{(0)} f_i^{(0)^3}}\right] \quad (9)$$

$$K_{lat}^{(s)} S_{lat}^{(s)} = m_{lat} n_{lat} f_{lat}{}^3 \sum_i \frac{X_i K_{ii}^{(0)} S_{ii}^{(0)}}{m_i^{(0)} n_i^{(0)} f_i^{(0)^3}} \quad (10)$$

$$K_{lat}^{(s)} S_{lat}^{(s)^2} = m_{lat} n_{lat} f_{lat}{}^3 \sum_i \frac{X_i K_{ii}^{(0)} S_{ii}^{(0)^2}}{m_i^{(0)} n_i^{(0)} f_i^{(0)^3}} \quad (11)$$

For BCC structure: $m_{lat} = m_i^{(0)} = 8, n_{lat}$=2, $f_{lat} = \sqrt{3}/2$, $n_i^{(0)} = 2$ *and* $f_i^{(0)} = \sqrt{3}/2$. After calculation, the solid solution strengthening contribution of the alloy is 508 MPa, and the influence of grain size on the strength of the aged alloy is relatively small, but it has a significant impact on the toughness of the alloy. The correlation between grain size and alloy strength can also be directly observed through Hall Petch:

$$\sigma_{gb} = Kd^{-1/2} \quad (12)$$

Among them, K is the coefficient in the Hall Page formula, the value is shown in Table 2, d is the grain size. After calculation, the contribution of fine grain strengthening to the alloy is 65MPa.

$$\sigma_p = \frac{K_s}{L_s} \quad (13)$$

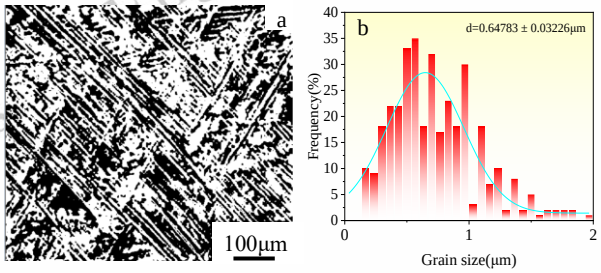

Fig.11 The SEM of the alloy after aging at 550℃/8h(a); binary processing diagram of the SEM of the alloy(b)

Ls is the spacing between secondary alpha phase particles, which can be obtained from the statistical graph of binary treatment based on SEM scanning results in Fig.11. Ks is a fitting parameter that the value is shown in Table 2. Where the average spacing of alpha phase in the microstructure after 550℃/8h aging is 0.648μm. After calculation, the contribution of aging strengthening at 550℃/8h is 440MPa.

Table 2 The parameter values of different strengthening model

parameter	*A*	*K* (*Mpa·m$^{-1/2}$*)	*Ks* (*MPa·μm^{-1}*)	*α*
Value	0.03596	0.4	285	10

Fig.12 shows the strengthening composition diagram of the alloy. It can be seen from the figure that solid solution strengthening and aging strengthening are the main strengthening methods of the alloy. The relative contributions of lattice resistance and grain boundary strengthening are relatively small, and the total calculated strength differs little from the theoretical value.

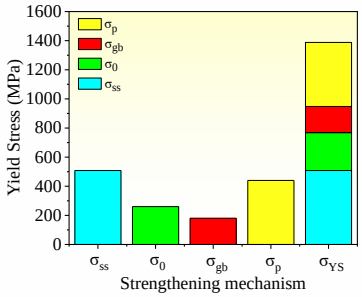

Fig.12 The yield strength composition diagram of the alloy.

4 Conclusion

1) A Ti-5.5V-4Mo-2.2Cr-Fe-3.6Al near beta type alloy was designed based on electron concentration, molybdenum equivalent, and Bo and Md values. The molybdenum equivalent of the alloy is a critical value of 10, and the position of the Bo Md value in the Bo-Md diagram shows that the alloy undergoes martensitic transformation during deformation.

2) The XRD and TEM results indicate that there is martensitic transformation in the microstructure of the alloy after 60% cold rolling. Due to the presence of martensite, the alloy obtains finer grain size after annealing and recrystallization during rolling process. The EBSD grain statistics show that the grain size of the alloy after annealing in the middle of the second rolling process is 38μm. The tensile results indicate that the yield strength of the alloy with a single BCC structure after annealing in the middle of the second rolling process is 1150MPa higher, and it has an elongation rate of more than 10.

3) The microstructure of the alloy after aging at 550℃/8 hours is relatively uniform, with a yield strength of 1500MPa and a 5% elongation. The strength of the alloy was simulated and calculated using different models, and the error between the result of the aged alloy at 550℃/8h and the experimental results was small.

References

1 Jiaqi Li, Duyao Zhang *et al*.*Journal of Materials Science & Technology*[J],2023,166:21-23

2 Yanlin Tong, Ke Hua *et al*.*Journal of Materials Science & Technology*[J],2024,196:200-214

3 Yipeng Gao, Yufeng Zheng *et al. Acta Materialia*[J],2020.196:488–504

4 Xiu-Qun,Wang *et al. Acta Materialia*[J],2022,227:117686

5 Tong Li, Damon Kent, Gang Sha *et al. Acta Materialia*[J], 2016,106:353-366

6 Tianlong Zhang, Dong Wang *et al. Acta Materialia*[J],2020,196:409–417

7 Fucheng Qiu Tuo Cheng *et al. Journal of Materials Science & Technology*[J],2024,171:24–36

8 Ahmad Chamanfar *et al*.*Journal of Materials Research and Technology*[J],2020,9(04):7721–7731

9 Feiyu Huang, Chaowen Huang *et al*.*Journal of materials research and technology*[J], 2023.26:7425-7443

10 Leticia F. Starck , Marcio Sangali *et al. Materials Letters*[J],2023,351:134968

11 张启飞，杨帅，稀有金属材料与工程[J],2022,51(7):2646-2653

12 王文婷，李沛，稀有金属材料与工程[J],2020,49(5):1707-1714

13 Jinguang Li, Keren Zhang *et al. Journal of Materials Research and Technology*[J],2024,28:4177–4185

14 Ke Hua, Yudong Zhang *et al. Acta Materialia*[J],2017,132:307-326

15 S. Sadeghpour *et al. Scripta Materialia*[J],2018,145:104-108

16 Chang-jiang Zhang, Xi Jiang *et al. Transactions of Nonferrous Metals Society of China*[J], 2022,32(04):1159−1168

17 B. Gu, P. Chekhonin, S.W. Xin *et al. Journal of Alloys and Compounds*[J],2021,876:159938

18 C.L. Zhang, X.Y. Bao *et al. International Journal of Plasticity*[J],2021,147:103126

19 Jinguang Li et al. *Journal of Materials Research and Technology* [J],2024,28:4177-4185

20 M. Coffigniez *et al. Materials & Design*[J],2024,239:112801

21 Feng Zhang *et al. Materials Characterization* [J],2024,208:113632

22 Jie Wang, Shuxin Bai *et al. Journal of Alloys and Compounds*[J].,2021,868:159190

23 M. Marteleur, F. Sun *et al*. Scr. Mater. *Scripta Materialia*[J], 2012, 66:749–752

24 G.L. Zhao, G. Wen, *et al. Materials Science and Engineering C* [J],2011,31: 106–113

通过成分设计和轧程中间退火工艺获得高强度近β型钛合金的研究

姜诗慧[1]，邸金南[2]，徐再东[3]，孙赛华[3]，毛萍莉[1]

(1. 沈阳工业大学，辽宁 沈阳 110870)

(2. 辽宁轨道交通职业学院，辽宁 沈阳 110230)

(3. 东北大学，辽宁 沈阳 110000)

摘　要：本文基于临界成分的多元合金化原则，结合电子浓度(VEC)、钼当量([Mo]eq) 和 Bo-Md 等衡量 β 相稳定性的参数设计了一种近 β 型 Ti-5.5V-4Mo-2.2Cr-Fe-3.6Al 合金。对均匀化处理后的试样进行轧程中间退火处理，最后对合金进行时效处理。光学显微镜(OM)、扫描电子显微镜(SEM)、X 射线衍射仪(XRD)、背散射电子衍射(EBSD)和透射电子显微镜(TEM)等技术用于分析合金在不同状态下的组织，同时对合金的室温拉伸性能进行测试。结果表明，在轧制过程中合金发生马氏体相变，由于马氏体阻碍晶界的迁移的作用，经过轧程中间退火后的合金获得了极其细小的晶粒的组织。中间退火后合金的晶粒度为 38μm，晶粒细化使得经过退火处理后的合金具有良好的强塑性匹配，拉伸屈服强度达到 1050MPa 同时延伸率达到 15%。经过时效处理后合金的组织中析出了大量细小而弥散的 α 相，细小 α 相的析出进一步提高了合金的性能，使合金的强度突破 1500MPa 并具有 4%以上的延伸率。

关键词：近β型钛合金；冷轧；退火；拉伸性能

作者简介：